VOL. 14, NO. 23, DECEMBER 2019 ISSN 1819-6608
ARPN Journal of Engineering and Applied Sciences

www.arpnjournals.com

OPTICAL ANALYSIS OF SOLAR RAYS ON FRESNEL LENSES COUPLED TO PARABOLIC CYLINDRICAL CONCENTRATOR RECEIVER

Angelica Palacios, Darío Amaya and Olga Ramos
Programa de Ingeniería en Mecatrónica, Universidad Militar Nueva Granada, Colombia
E-Mail: dario.amaya@unimilitar.edu.co

ABSTRACT

Fresnel lenses have been used as high concentration elements, in solar collection systems such as photovoltaic panels and collectors, to improve the optical and thermal efficiency; which in many cases don't present a good thermal behavior, due to the climatic conditions of study site. Therefore, this work presents the analysis of the incident ray optics on concentration lenses, coupled to parabolic cylindrical collector receiver tube, in Bogotá city; in order to improve the thermal transfer phenomena of the capture system. For this purpose, we calculated different solar angles that influence the incident rays on the Earth's surface, such as azimuth, zenith and slope, as a basis for obtaining the incident angles in the lens and then the respective refractive angles when concentrate, towards the focal spot (receiver). Subsequently, parameters such as thickness, focal length and its relation to the concentration factor of the lens were analyzed in order to validate the characteristics of the lens. Finally, the effective radiation on the collector system, as well as the thermal behavior of both the fluid and the solid, was evaluated through computational dynamic simulation. The solar angles, incidents and refracted in the Fresnel lens in the range between 6:00 am and 4:00 pm hours, in each month are presented in this work; from this the efficiency of the lens at midday was 82.5%, and specifically on the wedge of this one, an efficiency of 96.3% was obtained. Temperatures higher than 200 °C were reached in the fluid circulating in the receiver.

Keywords: solar power generation, energy capture, fresnel lens, solar collector, solar angles.

Nomenclature			
L	Length	μ_c	**Wedge efficiency**
W	Width	δ_m	Permissible half angle
f	Focal length	R_2	Position in x of the output ray
t_k	Thickness	R_c	Distance output ray and receiver
δ	Declination angle	C_o	Lens concentration
n	Day of the month	α_c	Acceptance half angle
ω	Hour angle	I_{Rad}	Solar radiation
β_1	Incidence angle	I_{ef}	Effective radiation
β_2	Refracted angle	l	Wedge length
β_3	Incident angle in the wedge	α_f	Wedge angle
β_4	Output angle	n_p	Refractive index
θ_z	Zenith angle	Subscript	
γ_s	Azimuth angle	cn	Concentrator
λ_a	Latitude	r	Receiver
ζ	Slope angle	l	Fresnel lens
I_{ef}	Effective radiation	mm	Minimum
μ_l	Lens efficiency	mx	Maximum

INTRODUCTION

One of the sources with greater capacity for use in renewable energy is the Sun; available and sustainable resource [1], [2]. Due to its high energy properties, numerous solar technologies have been developed such as photovoltaic and solar thermal systems; in the latter there are flat and parabolic collectors [3], [4]. Components such as Fresnel lenses, focal concentration systems, reflectors, central receivers, among others are used in these solar collection systems, [5], [6] in order to raise the temperature of a transfer fluid, [7]. Despite their great capacity for concentration, solar capture systems present energy losses associated with optical and thermal phenomena. The first is caused by the optical performance that depends on factors such as reflectance, absorptivity, transmittance and interception factor; while thermal losses are due to heat transfer by convection and radiation from the environment, [8]-[10] To improve the behavior of these systems, it is necessary to analyze the conditions of the study site and its influence on the parameters that intervene in the performance of the solar collector, some practical methods to evaluate the optical and thermal efficiency through practical and experimental tests have been proposed by [11]-[13]

As mentioned above, Fresnel lenses are part of the concentration systems, these are commonly used in solar applications, due to their high properties of optical efficiency, energy density, minimum volume, light weight

ARPN Journal of Engineering and Applied Sciences

and associated with this a low cost in the market, compared to large high concentration mechanisms [14] [15]. The operation of these lenses is based on the law of refraction of rays, through media with different densities; which allows diverting the initial direction of the light ray. The Fresnel lens is a modified conventional lens, which eliminates unwanted material and thereby reduces the losses by absorption, while reducing weight and quantity of material for manufacturing [16] [17]. Fresnel lenses have been studied in numerous works, one of them related to the use of optical devices in the solar control of buildings; The results in [18], present a collection between 60% and 80% of the solar radiation by means of Fresnel lenses focused on a linear absorber, which allows to distribute the light towards the interior of the space according to the needs of illumination and heating. On the other hand, in this work we propose the implementation of lenses in thermal energy absorption systems such as photovoltaic systems, with which we could achieve an approximate efficiency of 50% through thermal absorbers of low operating temperature.

The synergy between photovoltaic cells and Fresnel lenses has been one of the applications where the optical properties of the lens are highly usable to improve the efficiency of these solar collection systems. This is how in [19], a photovoltaic mechanism with a linear Fresnel lens was proposed, reaching a total efficiency of 53% compared to a previous thermal configuration, where a 46.6% efficiency was obtained. Similarly, the design and experimentation of a solar capture system by photovoltaic cells and Fresnel was carried out, this based on variable climatic conditions. With the above it was shown in [20] that cloudy weather directly affects electrical efficiency and has less effect in thermal efficiency. A study on the performance of a power plant with a capacity of $30KW$ was carried out [21], which had Fresnel optical concentrators, which achieved an efficiency of 25.8%; With the generated power it was possible to satisfy the 10% energy demand in places like Japan and Korea. Another application in the field of solar energy was developed in [22], where a greenhouse was validated with concentrators such as linear Fresnel optical devices and monocrystalline photovoltaic cells with tracking system; the electrical power output was 38 W/m^2, while the thermal power was 70 W/m^2.

Specifically for solar concentration systems, such as flat or cylindrical parabolic collectors, the effect of Fresnel lenses on the thermal properties of different cavities of a receiver of a collector has been studied as in [23]. In this work the optical diameters of the opening, the cavity and the receiving tube were obtained, as well as the vertex for the cross section of the receiver; within the conclusions it was found that the geometric concentration of the solar concentrator with the Fresnel lens should be higher than 500 to show an improvement in the thermal performance of the system. Another of the developments in concentration solar collectors with study lenses is found in [24], where a system with an approximate thermal efficiency of 50% is proposed at a transfer fluid temperature of 90°C. Through experimentation, it was calculated that the energy lost was $0.578W/m^2 K$, this is much lower than the results obtained in a previous validation of a vacuum tube collector without Fresnel concentration. The development carried out in [25], presents a solar collector by Fresnel concentration, designed with different cavity receiver architectures. The analysis of the optical properties was carried out by means of the Monte Carlo ray tracing method, whereby it was possible to obtain the radiation distribution and the impact of the angle of incidence on the optical performance of the collector. Within the conclusions of this work, it was found that the triangular architecture of the receiver reached the highest optical efficiency with 81.2%, while its thermal efficiency was 30% at 120 °C.

Finally in [26], the flow distribution of a Fresnel lens was studied by concentrating solar energy, by means of experimental tests. Through a photodetector and mapping the directions and positions of the flow in a plane were scanned. From this study it was identified that both the focal distance and the maximum flux density are key parameters to evaluate the distribution and selection of suitable components for the solar capture system. Based on these assessments, this work presents the results of optical and thermal analysis of incident solar rays on an array of Fresnel lenses coupled on a receiver of a parabolic cylindrical collector, to improve the thermal behavior of these systems in the climatic conditions of the city of Bogotá-Colombia.

METHODS

System description

A parabolic cylindrical concentrator consists of a solar capture system formed by a concentrating and receiving surface. In addition to these components, in this work the Fresnel lens was considered as a heat concentration element, to improve the thermal transfer phenomena of the system. The scheme in Figure 1 illustrates the system analyzed in this work.

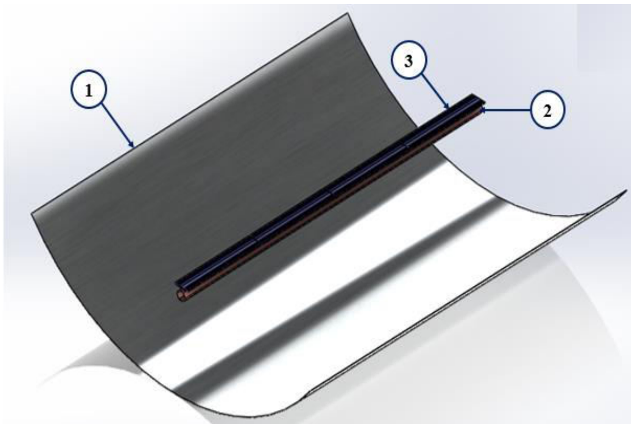

Figure-1. Solar collection system.

The components of the system are presented in Table-1.

ARPN Journal of Engineering and Applied Sciences

Table-1. System Components.

No	Component	Quantity
1	Concentrator	1
2	Receiver	1
3	Fresnel Lens	4

The concentrator as illustrated in Figure-2 is a reflective aluminum sheet with parabolic geometry.

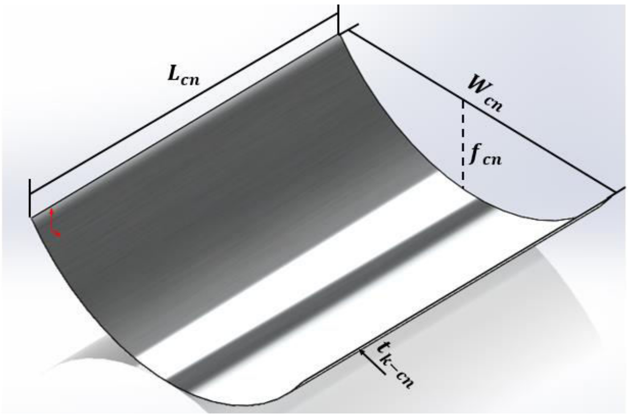

Figure-2. Concentrator surface.

The concentrator surface uses parabolic geometry to focus the solar rays on a point of concentration, distance known as focal distance. The characteristics and dimensions of the concentrator are presented in Table-2.

Table-2. Concentrator features.

Length	L_{cn}	$850mm$
Width	W_{cn}	$750mm$
Focal length	f_{cn}	$187.5mm$
Thickness	t_{k-cn}	$0.9\ mm$
Material	Aluminum	

The receiver tube of the system is illustrated in Figure-3.

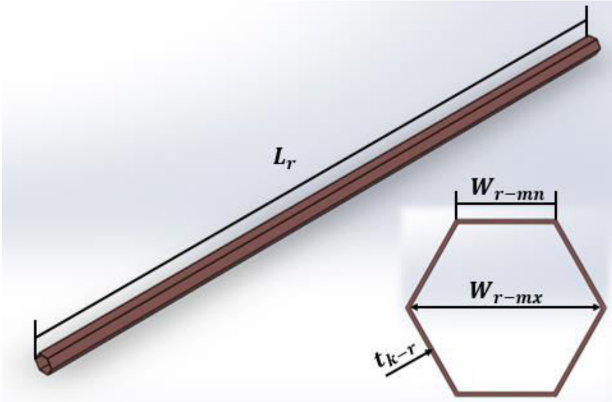

Figure-3. Receptor pipe.

The receiving surface consists of a tube with high thermal properties, which transfers energy in heat form to the fluid conducted inside. The characteristics and dimensions of the receiver are presented in Table-3.

Table-3. Hexagonal pipe features.

Length	L_r	$800\ mm$
Width min	W_{r-mm}	$11.60\ mm$
Width max	W_{r-mx}	$23.19\ mm$
Thickness	t_{k-r}	$0.5mm$
Material	$Cooper$	

For the development of this work, three fundamental aspects of analysis, solar resource, Fresnel lens and light optics were considered. The first one is the description of the solar resource in the place of study, for this case Bogotá Colombia; in this, the angles of the solar rays that arrive on the surface of the earth and affect the thermal system, composed of the concentrator, receiver and Fresnel lens described above were identified.

Solar resource description

The sun position with regard to incident solar radiation on the ground and a study plane, with any orientation relative to the earth and at any time; it can be described in terms of angles such as latitude, declination, time, azimuth, zenith and incidence [27]. Figure-4 shows the declination angle [$\boldsymbol{\delta}$], which is the position of the sun at solar noon, the hour angle [$\boldsymbol{\omega}$] is the angular displacement of the sun due to the rotation of the earth on its axis, with a variation of 15° per hour; and the angle of incidence [$\boldsymbol{\beta_1}$], angle between the beam radiation the surface and the normal to it.

VOL. 14, NO. 23, DECEMBER 2019 ISSN 1819-6608
ARPN Journal of Engineering and Applied Sciences

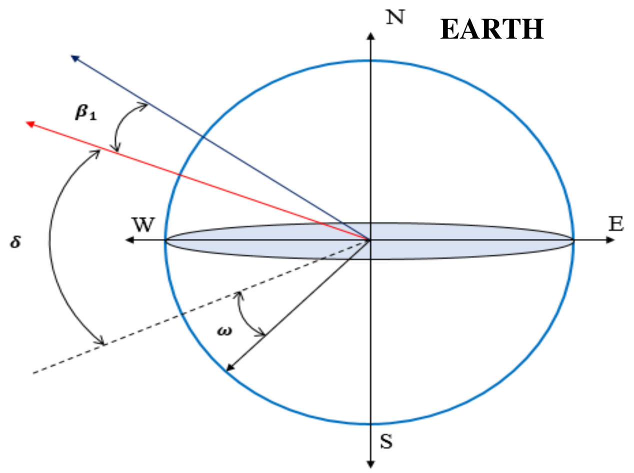

Figure-4. Declination, Hour and incidence angles on Earth.

The declination angle [$\boldsymbol{\delta}$],, can be calculated through the Cooper approximation [28], as described in Ec. (1) where the day number of the month [$\boldsymbol{n}$], is related, taking into account the number average of days in each month of the year, recommended by [29].

$$\delta = 23.45° \ \sin(360° \times \frac{284+n}{365}) \quad (1)$$

In the expression of Ec. (2) the day hour [$\boldsymbol{h}$] is related to the variation of 15° per hour, to obtain the hour angle [$\boldsymbol{\omega}$].

$$\omega = 15° \times (h - 12) \quad (2)$$

Furthermore, the angle of incidence [$\boldsymbol{\beta_1}$] on the surface can be calculated from declination [$\boldsymbol{\delta}$] and hour [$\boldsymbol{\omega}$] angles. If the analysis surface has a unique adjustment, the angle [$\boldsymbol{\beta_1 = \beta_{1\mu}}$], is obtained through Ec. (3).

$$\beta_{1\mu} = \cos^{-1}((\sin\delta)^2 + (\cos\delta)^2 \cos\omega) \quad (3)$$

If the surface has a continuous adjustment during the day, in order to track solar, [$\boldsymbol{\beta_1 = \beta_{1c}}$] and can be calculated with Ec. (4).

$$\beta_{1c} = \cos^{-1}\left(\sqrt{1 - (\cos\delta)^2(\sin\omega)^2}\right) \quad (4)$$

Finally, the zenith angle [$\boldsymbol{\theta_z}$] and azimuth [$\boldsymbol{\gamma_s}$] can be described in the plane normal to the horizontal surface, as illustrated in Figure-5. The first is the angle between the vertical and the line to the sun, while the second consists of the angular displacement from the south of the beam radiation projection in the horizontal plane.

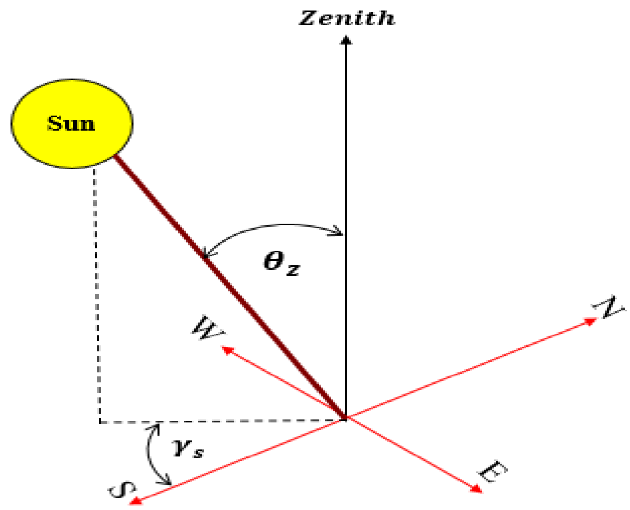

Figure-5. Normal plane over surface.

In Ec. (5) the declination angle [$\boldsymbol{\delta}$], hour angle [$\boldsymbol{\omega}$] and latitude [$\boldsymbol{\lambda_a}$] for this case $\lambda_a = 4.633°$ are related.

$$\theta_z = \cos^{-1}(\cos\lambda_a \cos\delta \cos\omega + \sin\lambda_a \sin\delta) \quad (5)$$

Similar to Figure-5, shows the azimuth angle [$\boldsymbol{\gamma_s}$], which is the angular displacement from the south of the ray projection on the horizontal plane. This angle, like the zenith [$\boldsymbol{\theta_z}$], is fundamental to obtain the slope angle [$\boldsymbol{\zeta}$], later implemented in the calculation of the effective radiation on the solar capture system [$\boldsymbol{I_{ef}}$].

$$\gamma_s = (sig(\omega) \times \left|\cos^{-1}\left(\frac{\cos\theta_z \times \sin\lambda_a - \sin\delta}{\sin\theta_z \cos\lambda_a}\right)\right| \quad (6)$$

The azimuth angle is possible to obtain it through the relation of Ec. (6), in this the hour angle sign is taken into account, as well as the zenith angle [$\boldsymbol{\theta_z}$], the declination angle [$\boldsymbol{\delta}$] and the latitude from the place of study [$\boldsymbol{\lambda_a}$].

Fresnel lens modeling

Unlike a conventional lens, the Fresnel lens is a thin optical device with concentric grooves on the surface known as wedges, in order to reduce weight and cost [30]. The lens concentrates the incident rays on its surface at a focal point, Figure-6.

ARPN Journal of Engineering and Applied Sciences

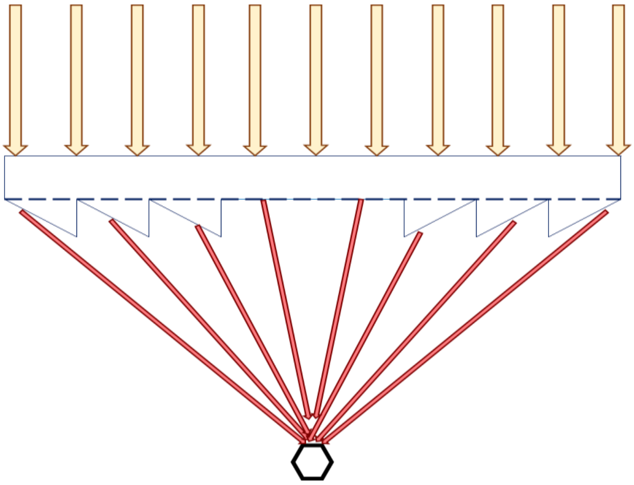

Figure-6. Concentration Rays on Fresnel lens.

For Fresnel lens design, parameters such as length, focal length, thickness, length of the wedge and angle of the tooth wedge are taken into account [31]. In this work, a linear Fresnel lens available on the market was selected, considering the best fit with the designed receiver. Figure-7 illustrates the lens sizing parameters.

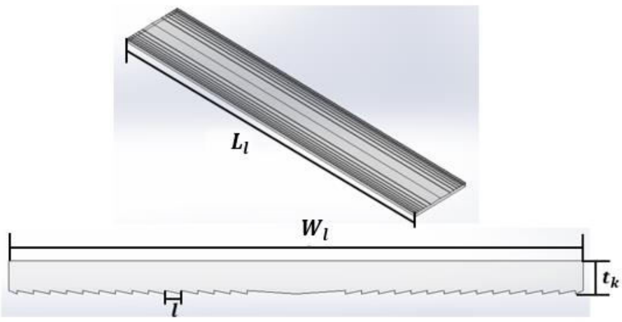

Figure-7. Lens Dimensions.

The dimensions and other relevant parameters of the lens modeled through the Optic Studio software are presented in Table-4.

Table-4. Lens Dimensions.

Length	$[L_l]$	**200** mm
Width	$[W_l]$	35 mm
Focal Length	$[f]$	12 mm
Thickness	$[t_k]$	2 mm
Wedge Length	$[l]$	1.54 mm
Wedge Angle	$[\alpha_f]$	70.62°
Refractive index	$[n_p]$	1.48
Material	*PMMA*	

Rays optics

After Fresnel lens modeling, optical analysis of rays was carried out on it. The solar ray strikes the lens surface at an angle $[\boldsymbol{\beta_1}]$ described above; this ray is refracted on the surface at an angle $[\boldsymbol{\beta_2}]$; therefore the angle of the ray that hits the surface of the wedge $[\boldsymbol{\beta_3}]$; is again refracted by exiting the lens at an angle $[\boldsymbol{\beta_4}]$. As shown in Figure-8.

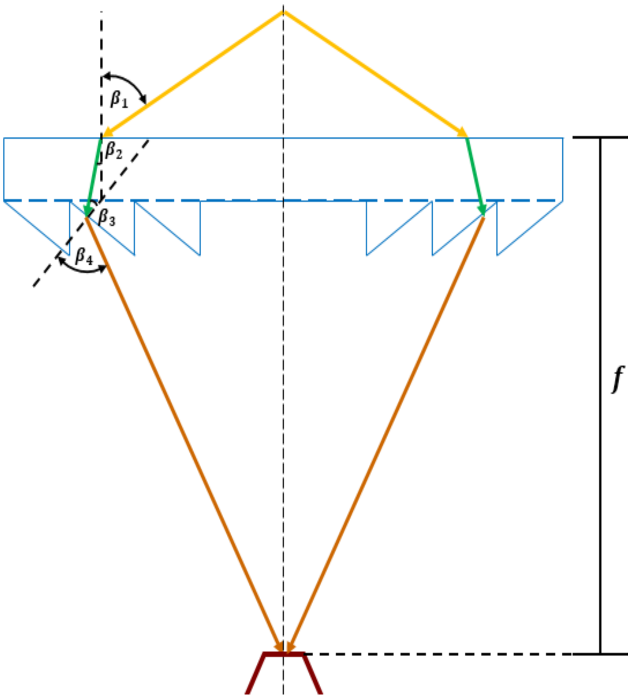

Figure-8. Solar ray angles on lens.

The angle $[\boldsymbol{\beta_2}]$ refracted on the surface of the lens can be calculated as in Ec. (7), based on refraction phenomenon being $[\boldsymbol{n_a}]$ air refractive index and $[\boldsymbol{n_p}]$ lens material refractive index.

$$\beta_2 = \sin^{-1}\left(\frac{n_a}{n_p}\sin(\beta_1)\right) \qquad (7)$$

When the ray is refracted, it strikes the surface of the wedge at an angle $[\boldsymbol{\beta_3}]$, which is obtained from the angle $[\boldsymbol{\beta_2}]$ and the wedge angle $\varphi = 70.62°$, as in Ec. (8).

$$\beta_3 = \cos^{-1}(\cos(\varphi)\cos(\beta_2)) \qquad (8)$$

The ray concentrated by the lens according to its focal distance $[\boldsymbol{f}]$, comes out with an angle $[\boldsymbol{\beta_4}]$, refracted by the surface of the wedge and therefore the refractive indexes are taken into account, as in Ec. (9).

$$\beta_4 = \sin^{-1}\left(\frac{n_a}{n_p}\sin(\beta_3)\right) \qquad (9)$$

Once the angles of the ray were defined throughout its trajectory in the lens, the relations in Ec. (10) were established to obtain the transmission efficiency of the lens.

ARPN Journal of Engineering and Applied Sciences

$$\begin{aligned}\beta_m &= \beta_1 + \beta_2\\ \beta_n &= \beta_1 - \beta_2\\ \beta_o &= \beta_3 + \beta_4\\ \beta_r &= \beta_3 - \beta_4\end{aligned} \quad (10)$$

The transmission efficiency on the surface of the lens [$\boldsymbol{\mu_l}$], is obtained by Ec. (11) through the relations of the previous angles.

$$\mu_l = 1 - \frac{\left[\frac{(\tan\beta_n)^2}{(\tan\beta_m)^2} + \frac{(\sin\beta_n)^2}{(\sin\beta_m)^2}\right]}{2} \quad (11)$$

Similarly, in Ec. (12) the calculation of the efficiency of the transmission on each wedge of the Fresnel lens [$\boldsymbol{\mu_c}$] is presented.

$$\mu_c = 1 - \frac{\left[\frac{(\tan\beta_r)^2}{(\tan\beta_o)^2} + \frac{(\sin\beta_r)^2}{(\sin\beta_o)^2}\right]}{2} \quad (12)$$

In addition to the calculation of the angles of the beam, in this work the positions in x of the output ray were considered and with it the distance between the point of the wedge and the point where it is concentrated on the receiver tube. These relationships together with the permissible e sun half angle [$\boldsymbol{\delta_m}$], are illustrated in Figure-9.

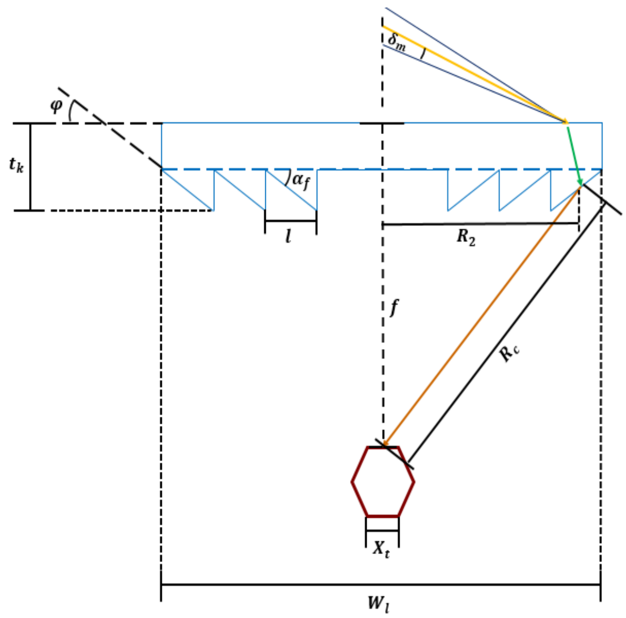

Figure-9. Output ray distances.

The calculation of the position in x of the output beam [$\boldsymbol{R_2}$], is obtained with Ec. (13), where [$\boldsymbol{t_k}$] is the thickness of the lens, [$\boldsymbol{l}$] the length of the wedge and [$\boldsymbol{\alpha_f}$] the internal angle of the wedge.

$$R_2 = \frac{(f - t_k) + (l \times \tan(\alpha_f/2))}{\tan(\beta_4)} \quad (13)$$

The distance between the point of departure of the ray and point of concentration on the receiver [$\boldsymbol{R_c}$], is obtained through the Euclidean distance Ec. (14) where it is related [R_2] calculated previously.

$$R_c = \sqrt{(R_2)^2 + \left(f - t_k + \tan(\alpha_f/2)\right)^2} \quad (14)$$

From the distances of the output ray, it is possible to obtain the concentration of this on the receiving surface [$\boldsymbol{C_o}$], as they are presented in Ec. (15), in this the admissible average solar angle is taken into account $\delta_m = 0.2667°$.

$$C_o = \frac{W_l}{(2R_c\tan(\delta_m)\tan(\beta_4))} \quad (15)$$

Incident-Effective radiation

To obtain the effective radiation incident on the Fresnel lens or on the concentrator surface, it must be analyzed if the beam is between an admissible ranges. For this, it is initially required to obtain the angle that is between the plane of the surface and the horizontal angle, known as slope [$\boldsymbol{\zeta}$], as presented in Ec. (16).

$$\zeta = \tan^{-1}(\tan\theta_z \times |\cos\gamma_s|) \quad (16)$$

From the angle [$\boldsymbol{\zeta}$], the limits of the range Ec. (17); are defined; where the angle of the beam will be evaluated having an acceptance half angle $\alpha_c = 11.75°$.

$$\begin{aligned}x_{mn} &= \zeta - \alpha_c\\ x_{mx} &= \zeta + \alpha_c\end{aligned} \quad (17)$$

The angle of the ray is obtained in a similar way to the angle [$\boldsymbol{\zeta}$], however, in this the sign of the cosine of the angle [$\boldsymbol{\gamma_s}$] is taken into account as in Ec.(18).

$$x = \tan^{-1}(\tan\theta_z \times \cos\gamma_s) \quad (18)$$

Once the angle [$\boldsymbol{x}$], is obtained, it is validated with Ec. (19) if it is in the range of the acceptable angle; if this is the factor [$F = 1$], if the angle is outside the range there will be no radiation incident at this moment on the system and therefore [$F = 0$].

$$\begin{cases} if\ x \geq x_{mn}\ and\ x \leq x_{mx}\ F = 1 \\ \quad otherwise\ F = 0 \end{cases} \quad (19)$$

Finally, the effective radiation over the aperture is calculated as in Ec. (20) with solar radiation [I_{Rad}].

$$I_{ef} = F \times I_{Rad} \times \cos(\beta_1) \quad (20)$$

RESULTS AND DISCUSSION (M_HEADING1)

Solar angles

The results of the optical angles are presented below, according to the Solar Resource in Bogotá-Colombia. Initially, the declination angle was obtained for each month of the year, Table-5. For the month of January

VOL. 14, NO. 23, DECEMBER 2019 ISSN 1819-6608
ARPN Journal of Engineering and Applied Sciences

www.arpnjournals.com

and December, lower angles were reached, while in June the highest angle was reached in the year.

Table-5. Declination angle obtained.

Month	Declination Angle
January	-20,917
February	-12,955
March	-2,418
April	9,415
May	18,792
June	23,086
July	21,184
August	13,455
September	2,217
October	-9,599
November	-18,912
December	-23,050

The angle of decline with respect to the months of the year, presented a Gaussian behavior Figure-10, where negative values of the angle are presented in the first and last three months of the year (January, February, March-October, November and December). The upward trend of the curve was presented in the months of May and April; while the bearish trend in the months of July and August. Finally, the distribution of the declination angle was found in the month of June with an angle of 23.086°.

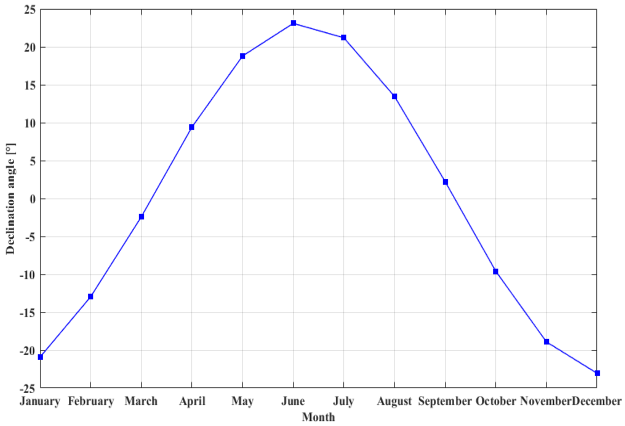

Figure-10. Declination angles for each year month.

For a range of daily hours between 6:00 a.m. to 4:00 p.m., the hour angle was calculated, considering the increase of 15° per hour. As expected, in the morning hours this angle is negative and from the middle of the day the angle is positive, being 61° the maximum value reached at 4:00 pm. These results are presented in Table-6.

Table-6. Hour Angle calculated.

Daily Hour	Hour Angle
6:00 a. m.	-89
7:00 a. m.	-74
8:00 a. m.	-59
9:00 a. m.	-44
10:00 a. m.	-29
11:00 a. m.	-14
12:00 a. m.	1
1:00 p. m.	16
2:00 p. m.	31
3:00 p. m.	46
4:00 p. m.	61

The hour angle is increasing in each hour of the day, by a factor of 15° per hour. As illustrated in Figure-11, the hour angle graph has a linear behavior, with a minimum angle of -89° and a maximum angle of 61°.

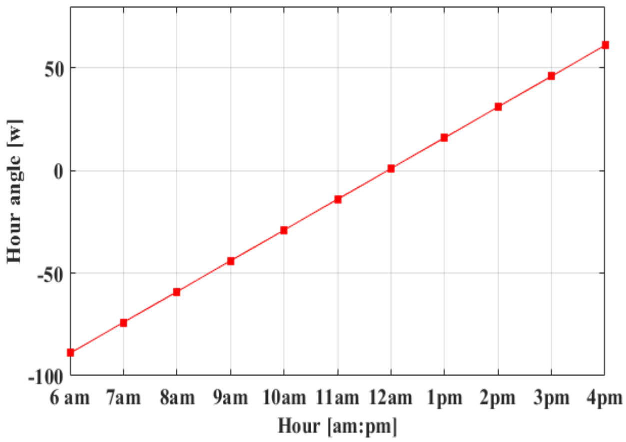

Figure-11. Hour angle for 6:00 am to 4:00 pm.

The results of the zenith angle for each month of the year and the proposed hours of the day are presented in Table-7. Although some differences are evident, the zentih angle has a similar behavior during the year. In the morning hours at 6:00 a.m., the angle is higher for each month and during the afternoons of the day it is decreasing until 12 o'clock; moment in which the angle increases again.

Table-7. Zenith Angle.

Month	Daily Hour										
	6am	7am	8am	9am	10am	11am	12am	1pm	2pm	3pm	4pm
January	90,72	76,83	63,21	50,14	38,24	29,01	25,57	29,99	39,72	51,84	65,00
February	90,07	75,54	61,17	47,11	33,75	22,42	17,62	23,71	35,46	48,95	63,08
March	89,20	74,27	59,37	44,53	29,82	15,66	7,12	17,47	31,77	46,50	61,35
April	88,26	73,49	58,69	43,90	29,16	14,69	4,88	16,58	31,12	45,87	60,66
May	87,56	73,37	59,20	45,19	31,65	19,68	14,19	21,08	33,40	47,04	61,09
June	87,27	73,48	59,74	46,27	33,53	22,88	18,48	24,07	35,15	48,04	61,56
July	87,40	73,42	59,48	45,75	32,64	21,41	16,58	22,70	34,33	47,56	61,33
August	87,95	73,38	58,80	44,27	29,93	16,39	8,88	18,08	31,82	46,20	60,74
September	88,82	73,88	58,93	43,98	29,05	14,18	2,61	16,15	31,04	45,97	60,92
October	89,79	75,08	60,48	46,09	32,21	19,93	14,27	21,37	34,01	47,99	62,42
November	90,56	76,48	62,65	49,30	37,01	27,28	23,57	28,33	38,55	51,04	64,47
December	90,89	77,22	63,85	51,09	39,60	30,87	27,70	31,79	41,02	52,74	65,61

Figure-12 In this, it is evident that in the months of March and April, the angle at noon is less approximately 18° with respect to the month of January, where a maximum value of 25.57° is reached. On the other hand, the months of February, May and June are within this interval, with an approximate average angle of 16°.

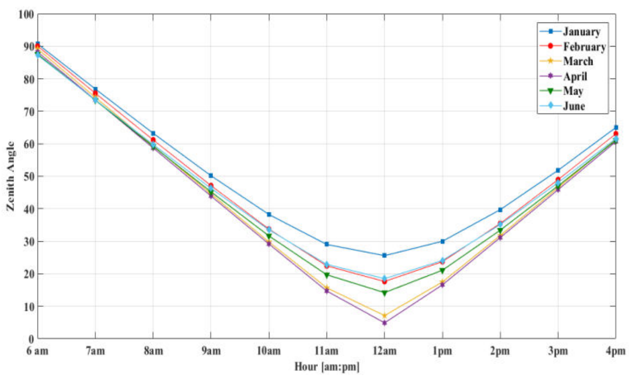

Figure-12. Zenith angle (January-June).

The graphs of the zenith angle for the following six months from July to December according to the time of day are shown in Figure-13. The behavior of the zenith angle of the following months is similar to the previous graphs; However, the months with an angle greater than half a day were November and December, with values of 23.57° and 27.70° respectively; while the months with lower values at that same hour were August with 8.88 ° and September with 2.61°. The zenith angle results allowed us to identify that this angle has higher values in the month of December and January at 6:00 a.m. and 4:00 p.m. Where the first reached an angle of 90.89 ° in the morning and 65.61° in the afternoon hours; the second month reached 90.72° in the early hours of the day and 65° in the afternoon. On the other hand, September recorded the lowest angles during the year at midday. In relation to the maximum angle in December has a difference of 90%.

VOL. 14, NO. 23, DECEMBER 2019 ISSN 1819-6608
ARPN Journal of Engineering and Applied Sciences

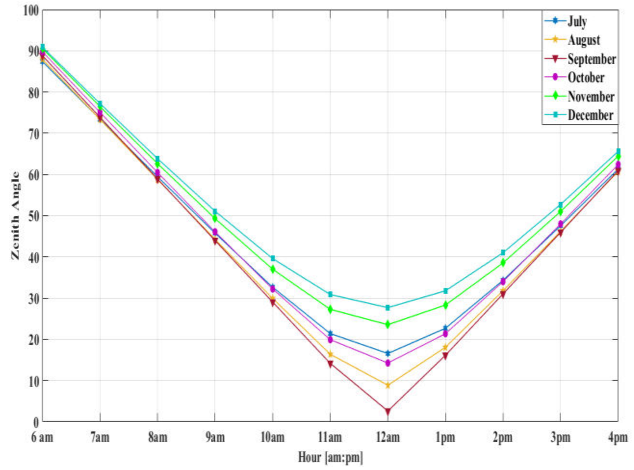

Figure-13. Zenith angle (July-December).

The next analyzed solar angle is the Azimuth, like the hour angle, this has negative values in the morning hours and positive in the afternoon. However, the change at noon has a more abrupt transition, changing for example in the month of June a value of -145.08 ° at 11 am to 177.10 ° at 12 noon. The results of the Azimuth angle between 6:00 a.m. to 4:00 p.m. for each month of the year is presented in Table-8.

Table-8. Azimuth Angle.

Month	Daily Hour										
	6am	7am	8am	9am	10am	11am	12am	1pm	2pm	3pm	4pm
January	-69,07	-67,24	-63,76	-57,71	-47,03	-27,78	2,16	31,01	48,84	58,72	64,34
February	-77,01	-75,34	-72,46	-67,52	-58,26	-38,18	3,22	41,93	59,90	68,36	72,94
March	-87,51	-86,17	-84,42	-81,79	-76,91	-63,53	8,09	66,52	77,80	82,23	84,69
April	-99,31	-98,46	-98,21	-98,77	-101,04	-109,76	168,33	107,64	100,56	98,63	98,21
May	-108,66	-108,25	-109,14	-112,03	-118,98	-137,15	176,14	133,49	117,66	111,48	108,93
June	-112,95	-112,72	-114,09	-117,83	-126,15	-145,08	177,10	141,56	124,62	117,14	113,80
July	-111,05	-110,74	-111,91	-115,29	-123,07	-141,84	176,73	138,23	121,62	114,65	111,65
August	-103,34	-102,68	-102,93	-104,56	-109,09	-123,49	173,69	120,26	108,19	104,23	102,84
September	-92,13	-90,97	-89,80	-88,39	-86,22	-80,66	22,48	81,93	86,59	88,60	89,96
October	-80,35	-78,77	-76,22	-71,93	-63,74	-44,41	4,00	48,23	65,22	72,65	76,64
November	-71,07	-69,27	-65,92	-60,09	-49,63	-29,95	2,37	33,33	51,43	61,07	66,48
December	-66,95	-65,09	-61,48	-55,23	-44,42	-25,71	1,98	28,78	46,23	56,27	62,09

For the months of January to June as shown in Figure-14, the angle variation in the first few hours of the day is in the range between -112.95 ° and -69.07 °, before noon (11:00 am) the variation is between -145.08 ° and -27.78 °; around midday (12:00 am) the angles are between 177.10 ° and 2.16 ° and finally in the afternoon hours the difference decreases in a range between 113.80 ° and 64.34 °.

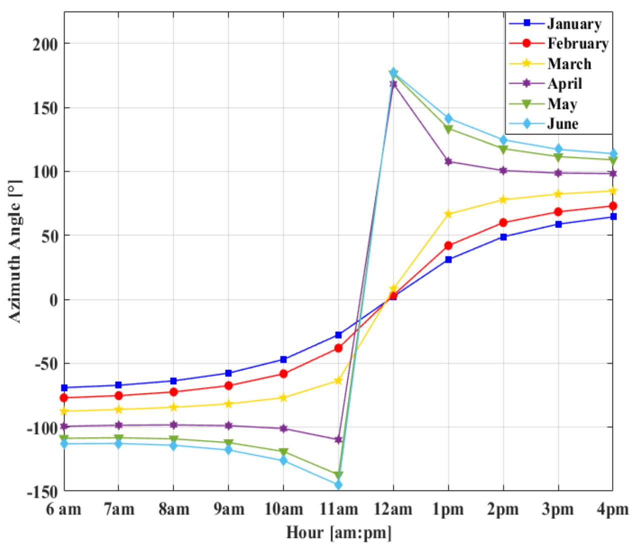

VOL. 14, NO. 23, DECEMBER 2019 ISSN 1819-6608
ARPN Journal of Engineering and Applied Sciences

Figure-14. Azimuth angle (January to June).

The azimuth angle of the months from July to December is illustrated in Figure-15. Through these, it is possible to show that the months of July and August as well as May and June, presented both the highest and the lowest values of the year, according to the time of day. The maximum value reached was 177.10°, while the minimum value was -145.08°.

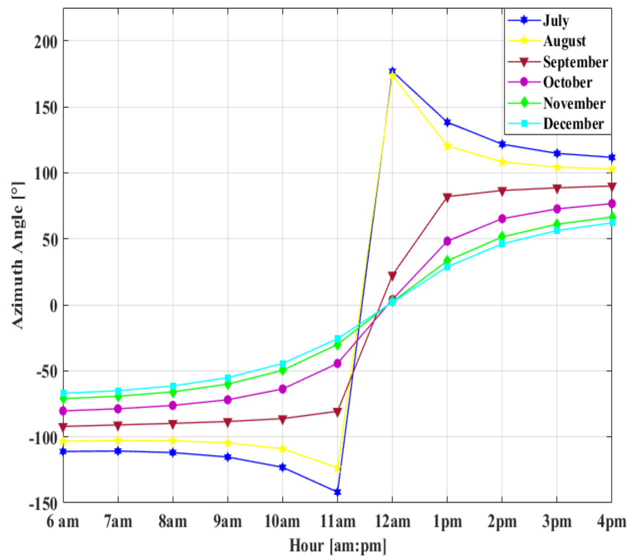

Figure-15. Azimuth angle (July to December).

Lens construction

Through the Optic Studio software, the modeling, construction and validation of the Fresnel lens was performed, considering the characteristics presented in Table-4. The lens generated as a virtual object is presented in Figure-16, where it is possible to visualize the concentration of the rays over the focal point through the lens surface.

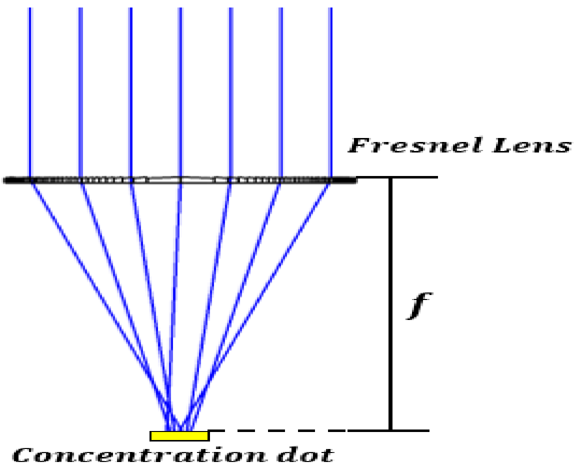

Figure-16. Fresnel lens constructed.

Concentrator-Fresnel lens assembly

Once the Fresnel lens was built, it was proceeded to perform the assembly with the concentration system, in the Solid Works software, as illustrated in Figure-17. Due to the size of the commercially available lens, it was necessary to assemble the four lenses to cover the entire upper surface of the receiver tube.

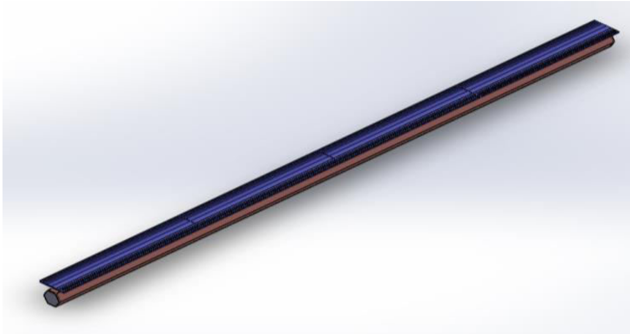

Figure-17. Receptor and Fresnel lens assembly.

The incident ray optics results on the lens and concentrates on the receiver are visualized in the following figures. Figure-18 shows the incidence of a single ray on the surface of the lens, then it is refracted towards the surface of the receiver and finally the ray emerges refracted to the exterior or concentrating surface.

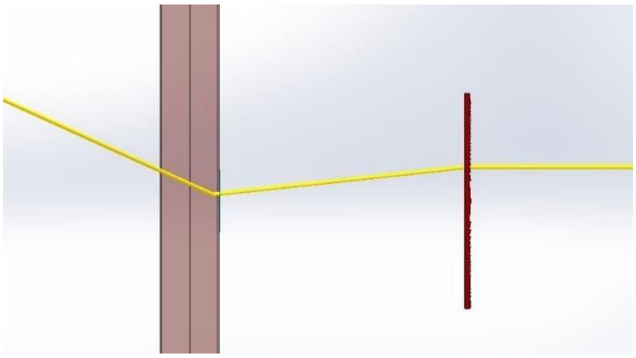

Figure-18. Single ray incident on the Fresnel lens.

To simulate multiple rays on the total surface of the lens array, four light sources were generated in the software, one for each lens. In Figure-19. A, the incidence of numerous rays on the lens and its concentration in the receiver tube of the concentrator system is shown in Figure-19. B.

(a)

 ISSN 1819-6608
ARPN Journal of Engineering and Applied Sciences

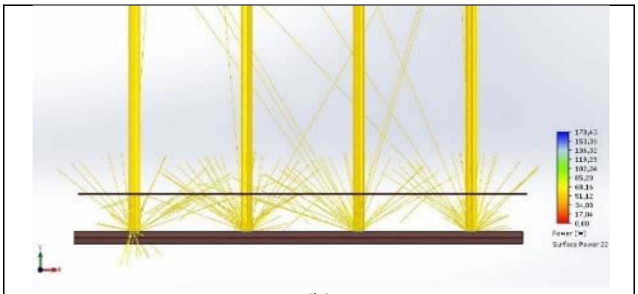

(b)

Figure-19. Multifold incident rays A) Light sources of incident rays. B) Concentrated and refracted rays on lens.

The results of the mathematical modeling of the direction of the rays presented in the simulation are described below. The incident angle $[\beta_{1\mu}]$ with unique adjustment for each hour of the day of the months from January to June is illustrated in the graphs in Figure-20. As shown, the incident angle for all months is always positive during the day, it gradually decreases linearly until it reaches midday, where its behavior transitions to a linear increasing state.

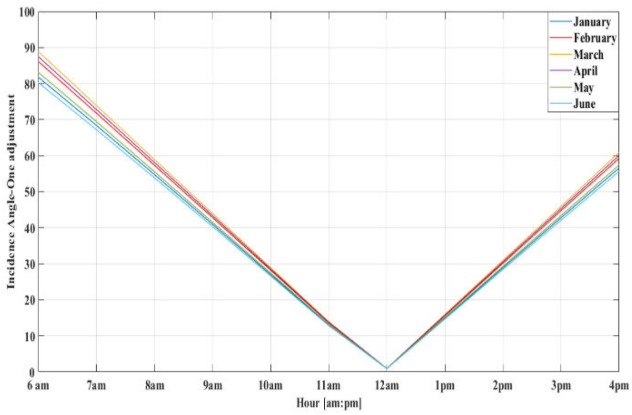

Figure-20. Incidence angle $[\beta_{1\mu}]$ results (January to June).

The incident angle with only adjustment for each hour of the day in the months between July to December of Figure-21, as for the months of January June, has an initially decreasing behavior before 12:00 am and then an increasing one. The maximum angles were obtained in the first hours of the day, in a range of [80.32° -87.49°] and at noon the angle decreased approximately 98.85% reaching a value of 0.92° in December.

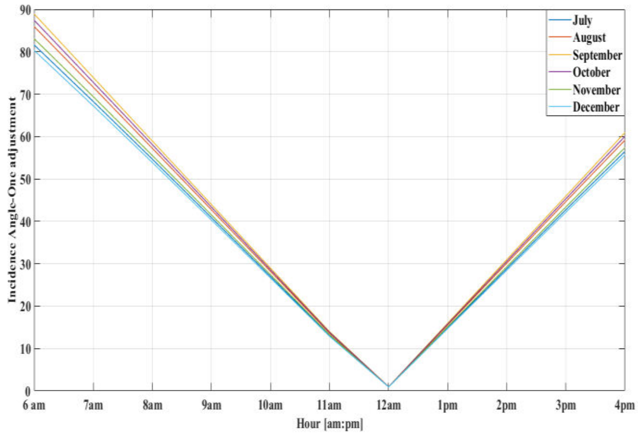

Figure-21. Incidence angle $[\boldsymbol{\beta}_{1\mu}]$ results (July to December).

As shown in Table-9, the variations of the months in a specific hour do not exceed 10%, this means the increase or decrease of the angle in 1° to 4°. However, the relevant variations occur during the day hours, where the angles of the afternoon tend to be the reflection of those in the morning.

Table-9. Incident angle one adjustment.

Month	Daily Hour										
	6am	**7am**	**8am**	**9am**	**10am**	**11am**	**12am**	**1pm**	**2pm**	**3pm**	**4pm**
January	81,80	68,41	54,77	40,96	27,05	13,07	0,93	14,94	28,91	42,81	56,60
February	86,17	71,82	57,36	42,82	28,25	13,64	0,97	15,59	30,19	44,76	59,29
March	88,90	73,92	58,94	43,96	28,97	13,99	1,00	15,99	30,97	45,96	60,94
April	87,49	72,84	58,13	43,38	28,60	13,81	0,99	15,78	30,57	45,35	60,09
May	83,14	69,46	55,57	41,54	27,42	13,25	0,95	15,14	29,31	43,42	57,43
June	80,30	67,23	53,87	40,32	26,63	12,87	0,92	14,71	28,46	42,13	55,67
July	81,62	68,27	54,66	40,89	27,00	13,05	0,93	14,91	28,86	42,73	56,49
August	85,95	71,65	57,23	42,73	28,19	13,61	0,97	15,56	30,13	44,67	59,16
September	88,92	73,94	58,95	43,97	28,98	13,99	1,00	15,99	30,98	45,96	60,95
October	87,43	72,80	58,09	43,35	28,59	13,80	0,99	15,77	30,56	45,32	60,06
November	83,07	69,41	55,53	41,51	27,40	13,24	0,95	15,13	29,29	43,39	57,39

VOL. 14, NO. 23, DECEMBER 2019 ISSN 1819-6608
ARPN Journal of Engineering and Applied Sciences

www.arpnjournals.com

December	80,32	67,25	53,89	40,33	26,64	12,88	0,92	14,72	28,47	42,14	55,68

It is also evident that when the sun is completely perpendicular to the radiation surface, the incident angle oscillates between 0.9 and 1. On the other hand, the incident angle with continuous adjustment, obtained for each hour of the day of the months between January to June is illustrated in Figure-22. Although the behavior of these results is like those obtained with the incident angle with only adjustment, the decrease in the angle and its subsequent growth are not linear; they adjust to a logarithmic curve of both descent and rise.

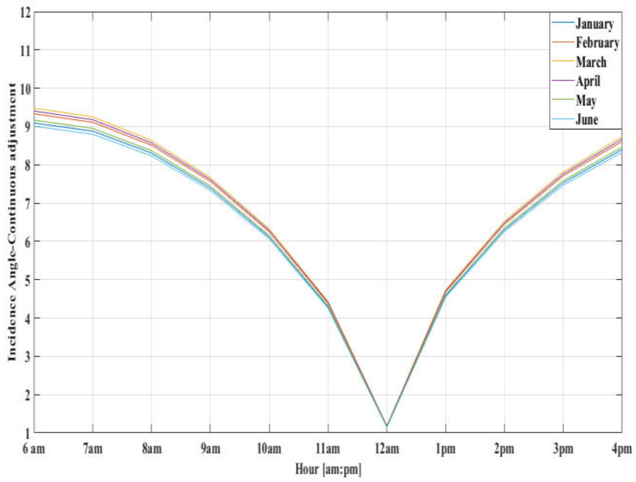

Figure-22. Incidence angle [β_{1c}] results (January to June).

Similarly, the graphs in Figure-23 show the results of the incident angle with continuous adjustment for each hour of the day of the months between July to December. As evidenced by the scale of these graphs, $\boldsymbol{\beta_{1c}}$is in a range of [1° - 10°], as it is a continuous adjustment the variation is small.

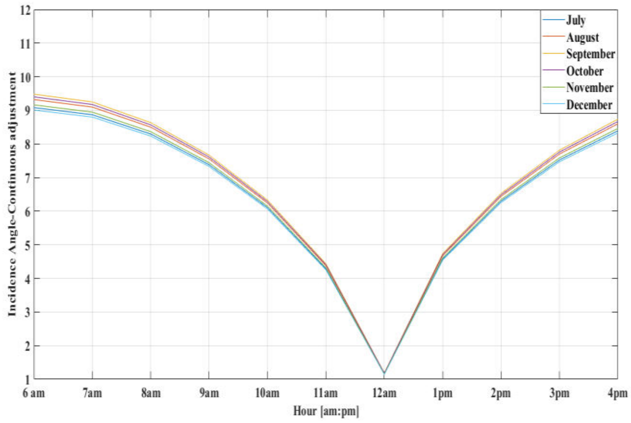

Figure-23. Incidence angle [β_{1c}] results(July to December).

The summary of the results of the incident angle β_{1c}during the year, for the place of study are recorded in Table-10. Considering the months with greater and lesser solar radiation, on the place of study; for the analysis of refractive angles and lens output, the months of September and December were selected to evaluate their behavior. The refractive angle obtained in each hour of the day from 6:00 a.m. to 4:00 p.m., is illustrated in Figure-24.

Table-10. Incident angle continuous adjustment.

Month	Daily Hour										
	6am	7am	8am	9am	10am	11am	12am	1pm	2pm	3pm	4pm
January	9,09	8,88	8,30	7,39	6,11	4,29	1,15	4,58	6,31	7,53	8,40
February	9,33	9,11	8,51	7,56	6,25	4,38	1,17	4,68	6,45	7,71	8,61
March	9,48	9,25	8,63	7,67	6,33	4,44	1,19	4,74	6,53	7,82	8,74
April	9,40	9,18	8,57	7,61	6,29	4,41	1,18	4,71	6,49	7,76	8,67
May	9,17	8,95	8,37	7,44	6,15	4,32	1,16	4,61	6,35	7,59	8,47
June	9,01	8,80	8,23	7,33	6,06	4,26	1,14	4,55	6,26	7,47	8,33

VOL. 14, NO. 23, DECEMBER 2019 ISSN 1819-6608
ARPN Journal of Engineering and Applied Sciences

www.arpnjournals.com

July	9,08	8,87	8,30	7,38	6,11	4,28	1,15	4,58	6,30	7,52	8,39
August	9,32	9,10	8,50	7,55	6,24	4,38	1,17	4,67	6,44	7,70	8,60
September	9,48	9,25	8,63	7,67	6,33	4,44	1,19	4,74	6,53	7,82	8,74
October	9,40	9,17	8,57	7,61	6,29	4,41	1,18	4,71	6,49	7,76	8,67
November	9,16	8,95	8,37	7,44	6,15	4,32	1,16	4,61	6,35	7,58	8,46
December	9,01	8,80	8,23	7,33	6,06	4,26	1,14	4,55	6,26	7,47	8,33

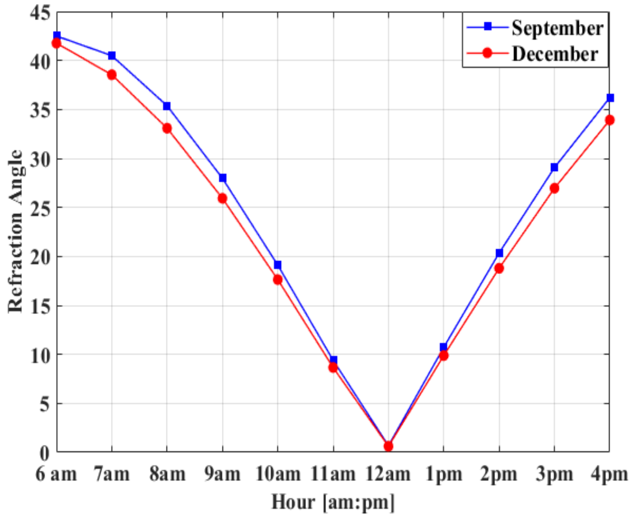

Figure-24. Refraction angle $\boldsymbol{\beta_2}$ results.

The maximum refracted angle is obtained for the month of September and December, at 6:00 a.m.; with a difference of 0.74° between them. As the hours pass, the angle decreases as $\boldsymbol{\beta_{1\mu}}$ varies; As expected, the lowest value of the results was obtained in both months at midday, where $\boldsymbol{\beta_2} = 0.68°$ for September and $\beta_2 = 0.62°$ in December. The comparison between these two points of analysis is presented in Table-11.

Table-11. Refraction angle$\boldsymbol{\beta_2}$.

Hour	$[\boldsymbol{\beta_2}]$ September	$[\boldsymbol{\beta_2}]$ December
6:00 a. m.	42,50	41,76
7:00 a. m.	40,49	38,54
8:00 a. m.	35,37	33,08
9:00 a. m.	27,97	25,93
10:00 a. m.	19,11	17,64
11:00 a. m.	9,40	8,66
12:00 a. m.	0,68	0,62
1:00 p. m.	10,73	9,88
2:00 p. m.	20,35	18,79
3:00 p. m.	29,06	26,96
4:00 p. m.	36,20	33,92

Similarly, the incident angle on the surface, $[\boldsymbol{\beta_3}]$ was calculated for the corresponding months. This angle showed a variation between 70° and 76°. As shown in Table-12, the difference between the value obtained in September and December was 0.16° at 6:00 am; while at 12:00 am the angle is the same for both months.

Table-12. Incidence angle β_3 results.

Hour	$[\boldsymbol{\beta_3}]$ September	$[\boldsymbol{\beta_3}]$ December
6:00 a. m.	75,838	75,670
7:00 a. m.	75,382	74,958
8:00 a. m.	74,301	73,857
9:00 a. m.	72,959	72,637
10:00 a. m.	71,727	71,565
11:00 a. m.	70,890	70,850
12:00 a. m.	70,621	70,621

The variation of the angle $\beta_3$between September and December is lower at 6:00 a.m. and 12:00 a.m., while in the interval of these hours the difference grows from 7:00 a.m. and as the hours pass decreases with the variation of β_2, Figure-25.

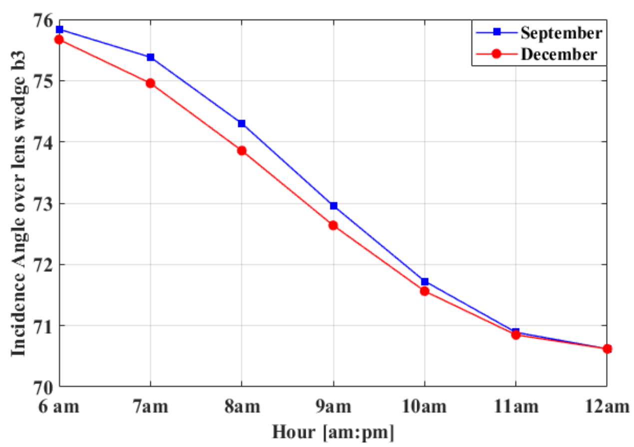

Figure-25. Incidence angle $\boldsymbol{\beta_3}$.

Finally, the angle of exit of the lens $[\boldsymbol{\beta_4}]$, obtained in the development of this work, is recorded in Table 13. For the months analyzed, the angle showed a variation between 39° and 41°. The maximum difference

VOL. 14, NO. 23, DECEMBER 2019 ISSN 1819-6608
ARPN Journal of Engineering and Applied Sciences

between September and December was 0.1° at 8:00 am, while the minimum difference was 0° at midday.

Table-13. Output angle β_4.

Daily Hour	$[\beta_4]$September	$[\beta_4]$December
6:00 a. m.	40,930	40,893
7:00 a. m.	40,829	40,732
8:00 a. m.	40,577	40,469
9:00 a. m.	40,241	40,157
10:00 a. m.	39,911	39,866
11:00 a. m.	39,676	39,664
12:00 a. m.	39,598	39,598

The graph of the exit angle for each of the months for 6 hours is presented in Figure-26. The behavior of $[\beta_4]$ is like that obtained in $[\beta_3]$, this is because the exit angle is the refraction of the angle incident on the wedge; therefore its variation is related to the results obtained.

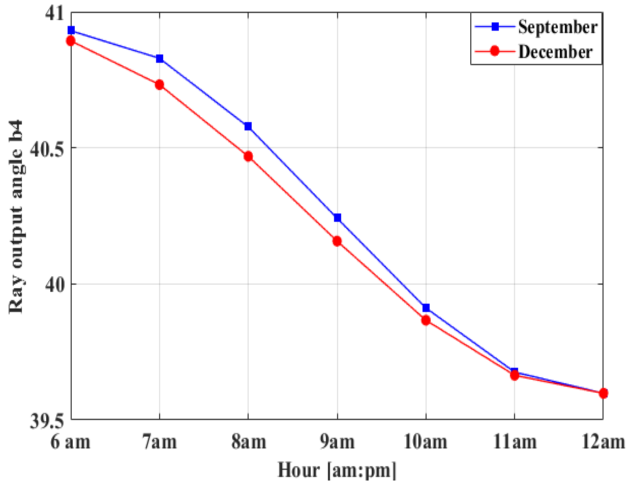

Figure-26. Output angle graphs.

After optical angles analysis, the efficiency of the lens and its wedge in the month of September is presented below, for different incident angles according to the time of day. The surface lens efficiency in Table-14, allows demonstrating that efficiencies greater than 90% are reached after 7:00 am and this is increased with the passing of the hours.

Table-14. Flux transmission efficiency on surface.

Hour	$[\beta_{1\mu}]$ September	μ_l
6:00 a. m.	88,92	0,104
7:00 a. m.	73,94	0,772
8:00 a. m.	58,95	0,919
9:00 a. m.	43,97	0,954
10:00 a. m.	28,98	0,961
11:00 a. m.	13,99	0,962
12:00 a. m.	1,00	0,963

The relationship between the incident angle with only adjustment and the efficiency of the lens on its surface is shown in Figure-27. As the incident angle $[\beta_{1\mu}]$ increases, the efficiency of the lens decreases, because the hours of the day where there is less radiation on the lens the angle is close to 90°, while with the passing of the hours, the angle decreases becoming completely normal on the surface with a value of 0° at midday.

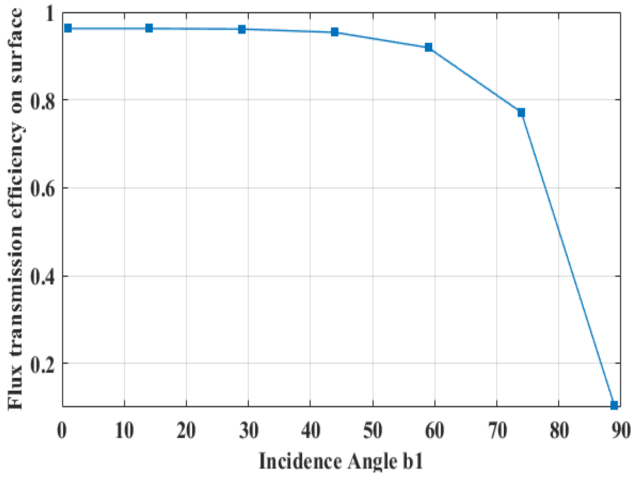

Figure-27. Efficiency on lens surface.

Because, on lens wedge, the angles vary due to the refraction phenomenon, the flow transmission efficiency on the wedge of the lens was also obtained for the month of September. The results are presented in Table-15, unlike the efficiency of the surface, on the wedge the efficiency is lower at 14.33% at noon, however it is evident that in the first hours 6:00 am, the efficiency is greater by 85.88%.

Table-15. Flux transmission efficiency on wedge.

Hour	$[\beta_{1\mu}]$ September	μ_c
6:00 a. m.	88,92	0,733
7:00 a. m.	73,94	0,743
8:00 a. m.	58,95	0,765
9:00 a. m.	43,97	0,789
10:00 a. m.	28,98	0,809
11:00 a. m.	13,99	0,821
12:00 a. m.	1,00	0,825

The efficiency ratio on the wedge of the lens with respect to the incident angle $\beta_{1\mu}$, is illustrated in Figure-28. Like the efficiency on the lens, as the incident angle increases the efficiency decreases, however for this case the factor of decrease is higher on the wedge than on the lens.

VOL. 14, NO. 23, DECEMBER 2019 ISSN 1819-6608
ARPN Journal of Engineering and Applied Sciences

www.arpnjournals.com

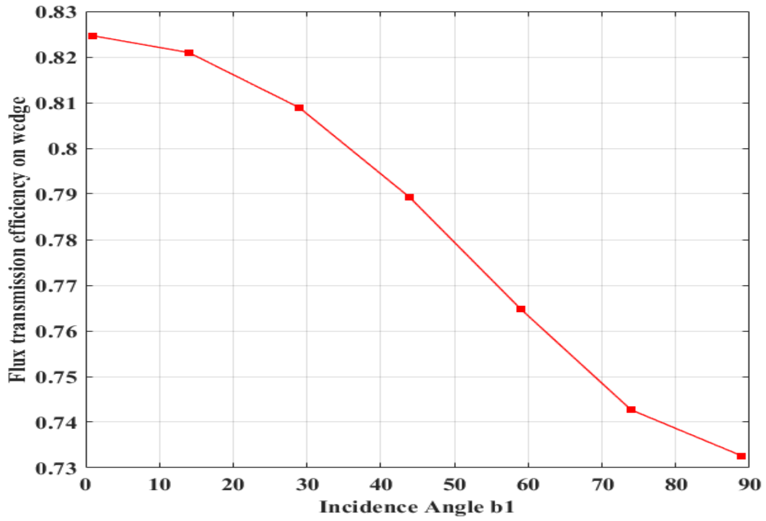

Figure-28. Efficiency on wedge surface.

Lastly optical analysis, the concentration factor of the lens was analyzed before the variation of parameters such as focal distance and thickness. With the first of them, focal lengths in a range between 40mm and 90mm were considered; the hours of analysis as well as the angles of departure were from 6:00 am to 12:00 am and the month consequently analyzed was September. For a commercial thickness of 2mm, the results obtained from the concentration factor are shown in Table-16.

Table-16. Lens concentration ratio based on focal length.

[β_4] September	Focal Length					
	40mm	50mm	60mm	70mm	80mm	90mm
40,930	74,26	58,87	48,76	41,62	36,30	32,18
40,829	74,38	58,96	48,84	41,68	36,35	32,23
40,577	74,66	59,18	49,02	41,84	36,49	32,35
40,241	75,03	59,48	49,27	42,05	36,67	32,52
39,911	75,40	59,77	49,51	42,25	36,85	32,67
39,676	75,66	59,97	49,68	42,40	36,98	32,79
39,598	75,74	60,04	49,73	42,44	37,02	32,82

As shown in the graph of Figure-29, the variation of the concentration factor with the increase in the exit angle on average was 1. However, when evaluating the behavior in each of the focal lengths, it is evident that between the smaller the focal length, the higher the concentration factor, specifically the study lens.

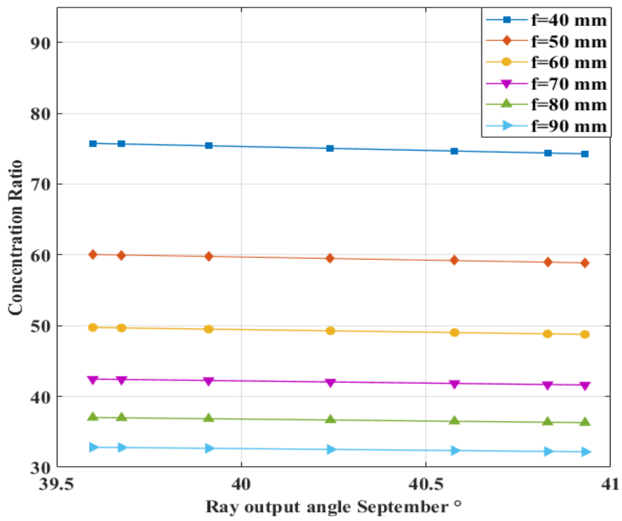

ARPN Journal of Engineering and Applied Sciences

Figure-29. Concentration ratio versus focal length change.

Furthermore, to calculate the concentration factor against the variation of the thickness in a range of 2mm to 5mm, a focal length of 60 mm was considered, distance obtained during the modeling of the lens as the optimum focus. As shown in Figure-30, the concentration factor decreases as the exit angle increases, and like the results obtained above, the average variation is approximately 1.

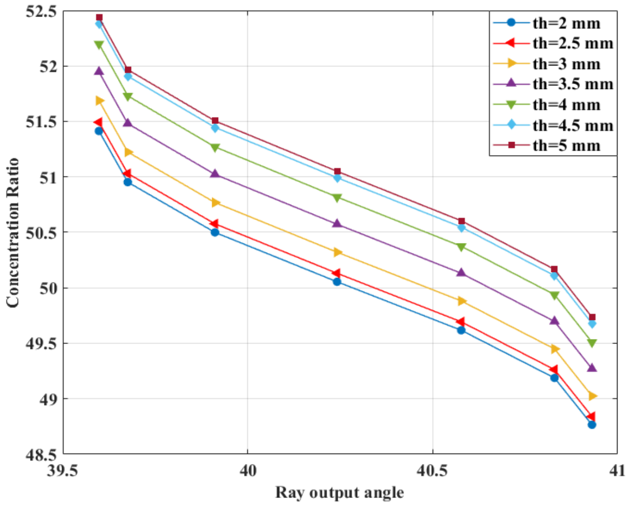

Figure-30. Concentration ratio versus thickness change.

Unlike the focal distance, the thickness of the lens generated not so relevant variations in the concentration factor; where the maximum value reached was 52.38 with a thickness of 5mm and with an exit angle of 39.67°. With the focal length of 60mm, the concentration factor was increased by increasing the thickness of the lens, as shown in Table-17.

Table-17. Lens concentration ratio based on thickness.

[β_4] September	**Lens Thickness (mm)**						
	2	**2,5**	**3**	**3,5**	**4**	**4,5**	**5**
40,930	48,76	49,19	49,62	50,05	50,50	50,95	51,41
40,829	48,84	49,26	49,69	50,13	50,57	51,03	51,49
40,577	49,02	49,45	49,88	50,32	50,77	51,22	51,69
40,241	49,27	49,69	50,13	50,57	51,02	51,48	51,95
39,911	49,51	49,94	50,37	50,82	51,27	51,73	52,20
39,676	49,68	50,11	50,55	50,99	51,44	51,91	52,38
39,598	49,73	50,17	50,60	51,05	51,50	51,97	52,44

Incident-Effective radiation

Finally, the effective radiation on the lens was calculated for each of the months of the year. The results are recorded in Table-18, where it is possible to show that with a direct radiation of 800[W/m^2], between 10:00 am and 5:00 pm, it will be widely usable; while at 6:00 am this radiation will oscillate between 15 [W/m^2] and 140[W/m^2], depending on the month.

Table-18. Effective beam radiation incident on the aperture [W/m2].

Month	Daily Hour										
	6am	7am	8am	9am	10am	11am	12am	1pm	2pm	3pm	4pm
January	114,15	294,37	461,48	604,09	712,48	779,27	799,89	772,96	700,30	586,86	440,38
February	53,47	249,63	431,53	586,76	704,74	777,43	799,88	770,57	691,48	568,00	408,56
March	15,36	221,54	412,72	575,87	699,87	776,28	799,88	769,06	685,94	556,16	388,58
April	35,00	236,02	422,41	581,48	702,38	776,87	799,88	769,84	688,79	562,26	398,88
May	95,53	280,64	452,29	598,77	710,10	778,70	799,89	772,23	697,59	581,07	430,62
June	134,82	309,61	471,68	609,99	715,12	779,89	799,90	773,77	703,30	593,28	451,22
July	116,60	296,18	462,69	604,79	712,79	779,34	799,89	773,06	700,65	587,62	441,67
August	56,52	251,88	433,04	587,63	705,13	777,52	799,88	770,69	691,92	568,95	410,16
September	15,14	221,38	412,61	575,81	699,85	776,27	799,88	769,06	685,90	556,09	388,46
October	35,82	236,62	422,82	581,72	702,49	776,90	799,88	769,87	688,91	562,52	399,31
November	96,54	281,39	452,79	599,06	710,23	778,73	799,89	772,26	697,74	581,39	431,14
December	134,46	309,34	471,50	609,89	715,07	779,88	799,90	773,76	703,25	593,17	451,03

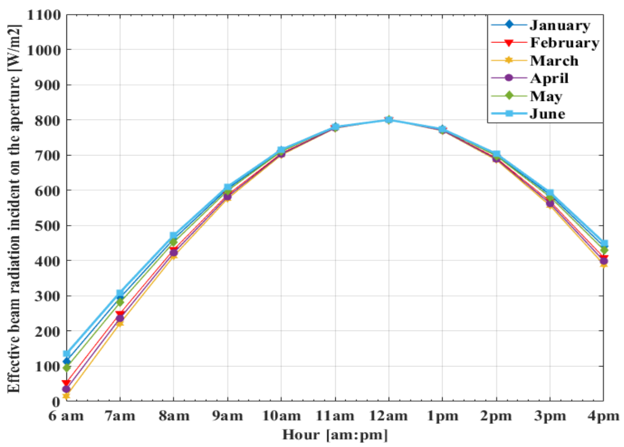

Figure-31. Effective radiation results (January to June).

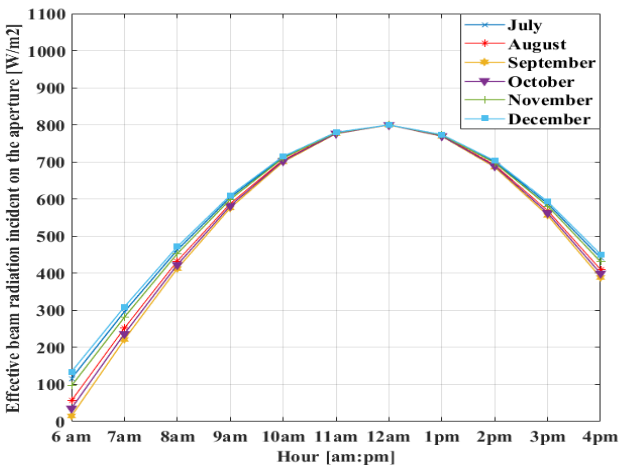

Figure-32. Effective radiation results (July to December).

Through Figure-31 and Figure-32 the behavior of the effective radiation is presented, where it is increased in the morning reached its maximum at noon and later it is decreased in the afternoon hours.

CFD THERMAL RESULTS

Using CFD computational tools, thermal parameters such as fluid temperature and solid were obtained. The processing required 64 iterations to find the solution of the system, in the first iterations the minimum temperature was at 20.028°C and the maximum at 155.76°C Figure-33, in this it is evident as the fluid Figure-33. A and the Receiver Figure 33.B increases its temperature thanks to the concentration of heat through the lens, without it raising its temperature. The heat distribution along the receiver tube is visualized in Figure-33. C where the temperature of the fluid is greatest between the receiver and the lens. The temperature of both solids and fluid are integrated in Figure-33. D, through this it is evident that both the external fluid and the direct face of the receiver receiving the concentration of the lens have the highest system temperature.

VOL. 14, NO. 23, DECEMBER 2019 ISSN 1819-6608
ARPN Journal of Engineering and Applied Sciences

www.arpnjournals.com

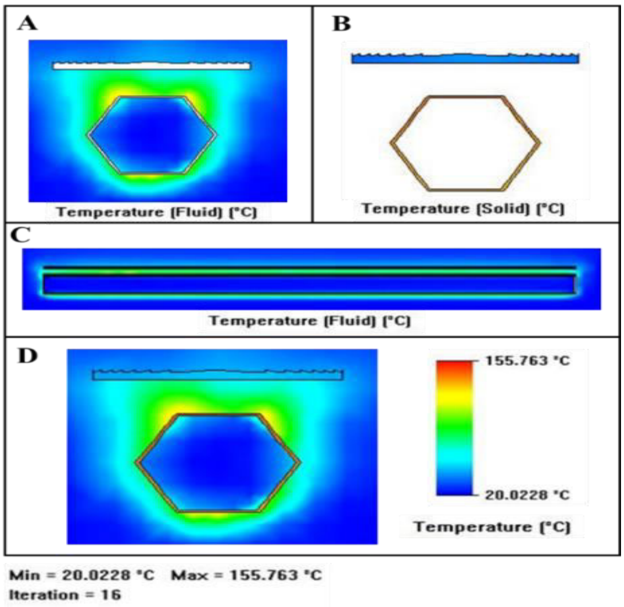

Figure-33. CFD results at iteration 16.

Similarly, Figure-34 shows the thermal results of both fluid and solids (lens and receiver) in iteration 46. These show the increase in temperature of the fluid over the focal point, as well as the distribution of heat in the receiver tube, the maximum temperature reached in this iteration was 225.36°C.

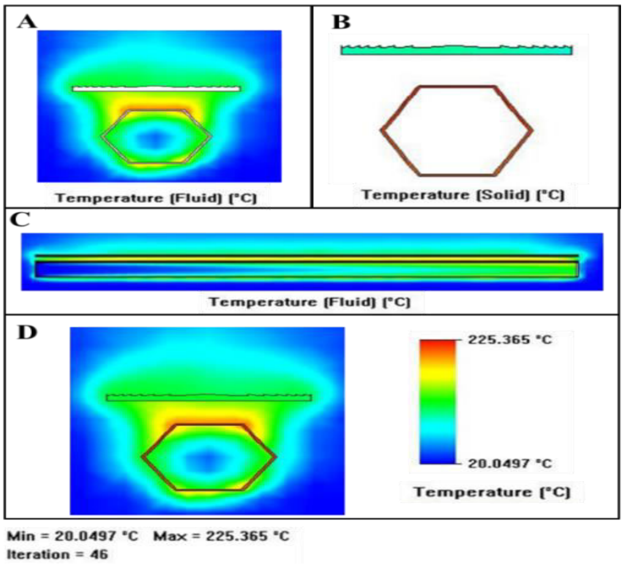

Figure-34. CFD results at iteration 46.

In the last iteration of the study by finite elements, the maximum temperature was 226,077°C, as illustrated in Figure-35, along the receiver tube there is evidence of a heat distribution with higher temperature at the outlet end of the fluid.

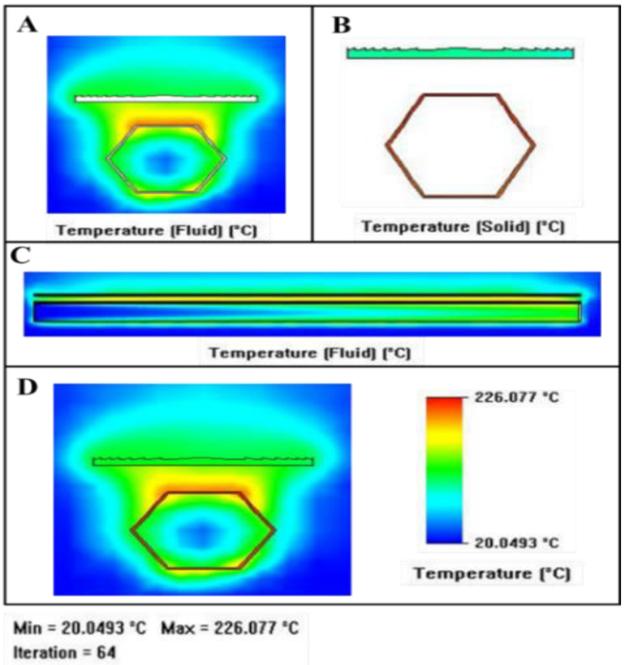

Figure-35. CFD results at iteration 64.

The curves of the maximum and average temperature of the solid obtained during the study are illustrated in Figure-36. From iteration 10, the increase of the temperature in each iteration is evidenced until it is established in the final value of 226°C. The average temperature of the solid reached its establishment at 150°C.

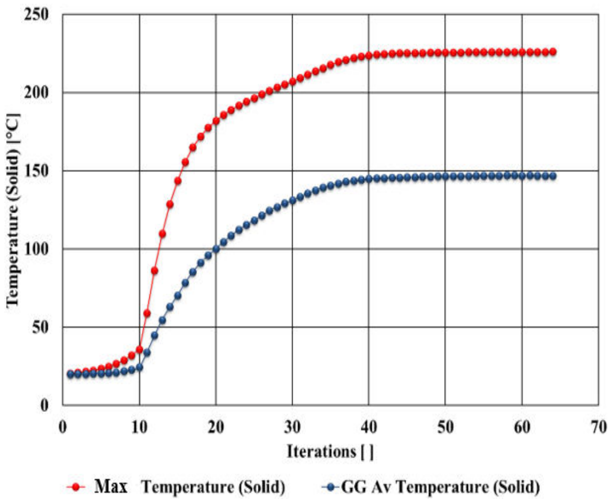

Figure-36. Solid Temperature.

Finally, the curve of maximum and average temperature of the fluid are presented in Figure-37, unlike the solid, the average temperature of the fluid was about 50°C and the maximum of 220°C.

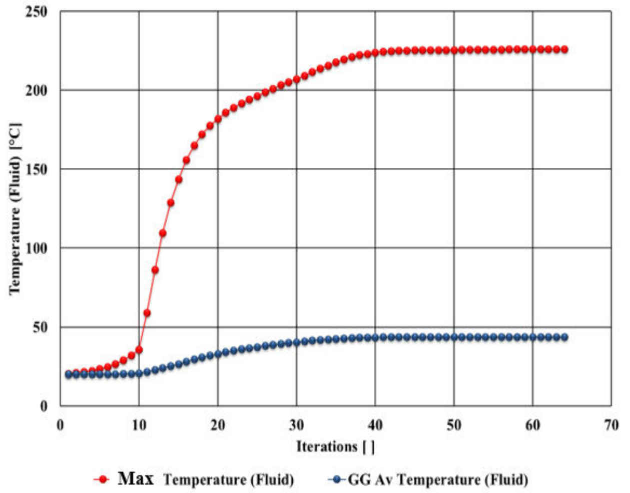

Figure-37. Fluid Temperature.

CONCLUSIONS (M_Heading1)

Through optical ray theory studied in this work, it was possible to identify the angles of the incident and refractive rays of the Fresnel lens, considering the solar resource in the city of Bogotá Colombia. On the solar half day, the incident angle is close to zero while for the first and last hours of the day the angle was greater. The above due to the movement of rotation of the earth that makes the sun travel from west to west the earth's surface.

The lens efficiency both in the surface and wedge, reached the maximum at midday with a value of 0.963 and 0.825 respectively; while the efficiency at 6:00 a.m. is lower with a value of 0.104 on the surface and on the wedge is 85.88% higher.

The lens concentration factor increased by varying the focal length of the lens, for this case the distance of 4mm reached a maximum value of 75.74, with a lens thickness of 2mm; for a focal length of 9mm, the concentration factor showed a decrease of 56.67% compared to 4mm at midday. On the other hand, by varying the thickness of the lens between 2mm to 5mm, the concentration shows approximate changes of 5.44% at 12:00 a.m.

The maximum temperature obtained during the simulation of the system by finite elements, was 226°C with a solar radiation of 800 W/m^2 and an effective radiation at noon of 799 W/m^2; therefore the Fresnel lens allowed to increase the initial temperature of the fluid approximately 198°C, by focusing the solar rays on a single point along the receiving tube.

ACKNOWLEDGEMENTS

The authors would like to thank the Nueva Granada Military University research center for financing this work (research project IMP-ING-2656, 2018).

REFERENCES

[1] M. Aramesh, F. Pourfayaz, and A. Kasaeian. 2017. Numerical investigation of the nanofluid effects on the heat extraction process of solar ponds in the transient step. Sol. Energy. 157: 869-879.

[2] M. Aramesh, A. Kasaeian, F. Pourfayaz, and D. Wen. 2017. Energy analysis and shadow modeling of a rectangular type salt gradient solar pond. Sol. Energy. 146: 161-171.

[3] D. A. Baharoon, H. A. Rahman, W. Z. W. Omar and S. O. Fadhl. 2015. Historical development of concentrating solar power technologies to generate clean electricity efficiently - A review. Renew. Sustain. Energy Rev. 41: 996-1027.

[4] H. L. Zhang, J. Baeyens, J. Degrève, and G. Cacères. 2013. Concentrated solar power plants: Review and design methodology. Renew. Sustain. Energy Rev. 22: 466-481.

[5] G. Wang, Z. Chen, P. Hu and X. Cheng. 2016. Design and optical analysis of the band-focus Fresnel lens solar concentrator. Appl. Therm. Eng. 102: 695-700.

[6] F. Duerr, Y. Meuret, and H. Thienpont. 2010. Miniaturization of Fresnel lenses for solar concentration: a quantitative investigation. Appl. Opt. 49(12): 2339.

[7] A. Kasaeian, S. Tabasi, J. Ghaderian and H. Yousefi. 2018. A review on parabolic trough/Fresnel based photovoltaic thermal systems. Renew. Sustain. Energy Rev. 91: 193-204.

[8] R. Wang, W. Qu, J. Sun, and H. Hong. 2017. An On-site Test Method for Optical Efficiency of Large-size parabolic trough Collectors. Energy Procedia. 105: 486-491.

[9] A. Alvarez, O. Cabeza, M. C. Muñiz and L. M. Varela. 2010. Experimental and numerical investigation of a flat-plate solar collector. Energy. 35(9): 3707-3716.

[10] Z. D. Cheng, Y. L. He, J. Xiao, Y. B. Tao and R. J. Xu. 2010. Three-dimensional numerical study of heat transfer characteristics in the receiver tube of parabolic trough solar collector. Int. Commun. Heat Mass Transf. 37(7): 782-787.

[11] C. Kutscher, F. Burkholder, and J. Kathleen Stynes. 2012. Generation of a Parabolic Trough Collector Efficiency Curve from Separate Measurements of Outdoor Optical Efficiency and Indoor Receiver Heat Loss. J. Sol. Energy Eng. 134(1): 011012.

[12] L. Valenzuela, R. López-Martín and E. Zarza. 2014. Optical and thermal performance of large-size parabolic-trough solar collectors from outdoor experiments: A test method and a case study. Energy. 70: 456-464.

[13] J. Pernpeintner, C. Happich, E. Lüpfert, B. Schiricke, N. Lichtenthäler and J. Weinhausen. 2015. Linear Focus Solar Simulator Test Bench for Non-destructive Optical Efficiency Testing of Parabolic Trough Receivers. Energy Procedia. 69: 518-522.

[14] R. Leutz, A. Suzuki, A. Akisawa, T. Kashiwagi and J. Toksoy. 2000. Developments and designs of solar engineering Fresnel lenses. Proc. Symp. Energy Eng. 2: 759-765.

[15] W. T. Xie, Y. J. Dai, R. Z. Wang and K. Sumathy. 2011. Concentrated solar energy applications using Fresnel lenses: A review. Renew. Sustain. Energy Rev. 15(6): 2588-2606.

[16] V. Kumar and R. Shrivastava. 2015. Fresnel lens: a promising alternative of reflectors in concentrated solar power. Sustain. SP Untawale -Renewable.

[17] N. Yeh. 2010. Analysis of spectrum distribution and optical losses under Fresnel lenses. Renew. Sustain. Energy Rev. 14(9): 2926-2935.

[18] Y. Tripanagnostopoulos, C. Siabekou and J. K. Tonui. 2007. The Fresnel lens concept for solar control of buildings. Sol. Energy. 81(5): 661-675.

[19] F. Karimi, H. Xu, Z. Wang, J. Chen and M. Yang. 2017. Experimental study of a concentrated PV/T system using linear Fresnel lens. Energy. 123: 402-412.

[20] C. Feng, H. Zheng, R. Wang and X. Ma. 2016. Performance investigation of a concentrating photovoltaic/thermal system with transmissive Fresnel solar concentrator. Energy Convers. Manag. 111: 401-408.

[21] K. Araki, T. Yano and Y. Kuroda. 2010. 30 kW Concentrator Photovoltaic System Using Dome-shaped Fresnel Lenses. Opt. Express. 18(S1): A53.

[22] P. J. Sonneveld, G. L. A. M. Swinkels, B. A. J. van Tuijl, H. J. J. Janssen, J. Campen and G. P. A. Bot. 2011. Performance of a concentrated photovoltaic energy system with static linear Fresnel lenses. Sol. Energy. 85(3): 432-442.

[23] W. T. Xie, Y. J. Dai and R. Z. Wang. 2012. Theoretical and experimental analysis on efficiency factors and heat removal factors of Fresnel lens solar collector using different cavity receivers. Sol. Energy. 86(9): 2458-2471.

[24] H. Zhai, Y. J. Dai, J. Y. Wu, R. Z. Wang, and L. Y. Zhang. 2010. Experimental investigation and analysis on a concentrating solar collector using linear Fresnel lens. Energy Convers. Manag. 51(1): 48-55.

[25] M. Lin, K. Sumathy, Y. J. Dai, and X. K. Zhao. 2014. Performance investigation on a linear Fresnel lens solar collector using cavity receiver. Sol. Energy. 107: 50-62.

[26] A. Ferriere, G. Rodríguez and J. Sobrino. 2004. Flux distribution delivered by a Fresnel lens used for concentrating solar energy. J. Sol. energy Eng. 126(1): 654-660.

[27] J. A. Duffie and W. A. Beckman, Solar engineering of thermal processes. Wiley, 2013.

[28] P. I. Cooper. 1969. The Absorption of Solar Radiation in Solar Stills. Sol. Energy. 12(3).

[29] S. A. Klein. 1977. Calculation of Monthly Average Insolation on Tilted Surfaces. Sol. Energy. Vol. 19.

[30] M. Miranda Herrara, V. Morales Ibarra, M. Duque Herrera, and C. González Sotelo. 2016. Calentador Solar con lente Fresnel. Rev. Prototipos Tecnológicos. Vol. 43.

[31] A. González García, Jorge Cordero Dávila, Alberto Santiago Alvarado and G. Castro. 2006. Diseño de una lente de fresnel de baja frecuencia usando trazo exacto de rayos. TEMAS Cienc. Y Tecnol. Vol. 10.